Monthly Notices
of the
ROYAL ASTRONOMICAL SOCIETY

Mon. Not. R. Astron. Soc. **417,** 2330–2346 (2011) doi:10.1111/j.1365-2966.2011.19414.x

General relativistic ray-tracing algorithm for the determination of the electron–positron energy deposition rate from neutrino pair annihilation around rotating neutron and quark stars

Z. Kovács⋆ and T. Harko⋆

Department of Physics and Center for Theoretical and Computational Physics, University of Hong Kong, Pok Fu Lam Road, Hong Kong SAR, China

Accepted 2011 July 8. Received 2011 July 8; in original form 2011 May 6

ABSTRACT

We present a full general relativistic numerical code for estimating the energy–momentum deposition rate (EMDR) from neutrino pair annihilation ($\nu + \overline{\nu} \rightarrow e^- + e^+$). The source of the neutrinos is assumed to be a neutrino-cooled accretion disc around neutron and quark stars. We calculate the neutrino trajectories by using a ray-tracing algorithm with the general relativistic Hamilton's equations for neutrinos and derive the spatial distribution of the EMDR due to the annihilations of neutrinos and antineutrinos around rotating neutron and quark stars. We obtain the EMDR for several classes of rotating neutron stars, described by different equations of state of the neutron matter, and for quark stars, described by the Massachusetts Institute of Technology (MIT) bag model equation of state and in the colour–flavour-locked (CFL) phase. The distribution of the total annihilation rate of the neutrino–antineutrino pairs around rotating neutron and quark stars is studied for isothermal discs and accretion discs in thermodynamical equilibrium. We demonstrate both the differences in the equations of state for neutron and quark matter and rotation with the general relativistic effects significantly modify the EMDR of the electrons and positrons generated by the neutrino–antineutrino pair annihilation around compact stellar objects, as measured at infinity.

Key words: dense matter – equation of state – stars: rotation.

1 INTRODUCTION

The neutrino–antineutrino annihilation processes may play an important role in many astrophysical phenomena. Hyperaccreting discs around neutron stars or magnetars, cooled from neutrino emission, could be the potential central engine of the gamma-ray bursts (GRBs) (Liu et al. 2010). The neutron star disc can cool more efficiently, and produce much higher neutrino luminosity and neutrino annihilation luminosity than its black hole counterpart with the same accretion rate. The neutron star surface boundary layer could increase the annihilation luminosity as well. An ultrarelativistic jet neutrino annihilation can be produced along the stellar poles. The role of the neutrino–antineutrino annihilation into electrons and positrons as the energy source of the GRBs has been intensively investigated in the literature (Paczynski 1990; Mészáros & Rees 1992; Ruffert & Janka 1998, 1999; Asano & Iwamoto 2002). The study of the electron energy deposition rate from the $\nu + \overline{\nu} \rightarrow e^+ + e^-$ neutrino annihilation reaction was initiated by Cooperstein, van den Horn & Baron (1986), Cooperstein, van den Horn & Baron (1987) and Goodman, Dar & Nussinov (1987), respectively. Neutrino–antineutrino annihilation into electrons and positrons can deposit more than 10^{51} erg above the neutrino-sphere of a Type II supernova (Goodman et al. 1987).

1.1 General relativistic effects on neutrino–antineutrino annihilation in black hole discs

For a full understanding of the effects of the neutrino annihilation in strong gravitational fields, general relativistic effects must be taken into account (Salmonson & Wilson 1999). In a Schwarzschild geometry, the efficiency of the $\nu + \overline{\nu} \rightarrow e^+ + e^-$ process is enhanced over the Newtonian values up to a factor of more than 4, in the regime applicable to Type II supernovae, and by up to a factor of 30 for collapsing neutron stars (Salmonson & Wilson 1999). The neutrino pair annihilation rate into electron pairs between two neutron stars in a binary system was obtained by Salmonson & Wilson (2001). The gravitational effects on neutrino pair annihilation near the neutrino-sphere and around the thin accretion disc around Schwarzschild and Kerr black holes were considered in Asano & Fukuyama (2000, 2001), respectively. The study

⋆E-mail: zkovacs@hku.hk (ZK); harko@hkucc.hku.hk (TH)

of the structure of neutron star discs based on the two-region (i.e. inner and outer) disc scenario was performed by Zhang & Dai (2009), who calculated the neutrino annihilation luminosity from the disc in various cases. As compared with the black hole disc, the neutrino annihilation luminosity above the neutron star disc is higher. The neutron star disc with the advection-dominated inner disc could produce the highest neutrino luminosity, while the disc with an outflow has the lowest (Zhang & Dai 2009).

General relativity and rotation cause important differences in the spatial distribution of the energy deposition rate by neutrino and antineutrino annihilation (Birkl et al. 2007). The energy–momentum deposition rate (EMDR) from the $\nu - \bar{\nu}$ collisions above a rotating black hole/thin accretion disc system was calculated by Miller et al. (2003) by imaging the accretion disc at a specified observer using the full geodesic equations, and calculating the cumulative EMDR from the scattering of all pairs of neutrinos and antineutrinos arriving at the observer. The dominant contribution to the EMDR comes from near the surface of the disc with a tilt of approximately $\pi/4$ in the direction of the disc's rotation. The EMDR at large radii is directed outwards in a conic section centred around the symmetry axis and is larger by a factor of 10–20 than the on-axis values. There is also a linear dependence of the EMDR on the black hole angular momentum. Other investigations of the general relativistic effects on neutrino propagation and annihilation were performed in Mallick & Majumder (2009) and Bhattacharyya et al. (2009). A general relativistic ray-tracing method for estimating the EMDR by neutrino pair annihilation in collapsars was developed recently in Harikae et al. (2010a). A special relativistic numerical scheme and code for estimating the energy and momentum transfer via neutrino pair annihilation was developed in Harikae, Kotake & Takiwaki (2010b).

1.2 $\nu\bar{\nu}$ annihilation processes in accretion discs around neutron stars

In most of the previous investigations of the neutrino annihilation processes the central compact object was assumed to be a black hole. A comparative study of the neutrino annihilation process from neutrinos emitted by accretions discs around neutron and quark stars was initiated in Kovács, Cheng & Harko (2010), and further developed in Kovács, Cheng & Harko (2011). In these studies the electron–positron energy deposition rate was obtained in the equatorial plane and along the rotation axis of neutron and quark stars, described by several equations of state. The differences in the equations of state for neutron and quark matter also have important effects on the spatial distribution of the energy deposition rate by neutrino–antineutrino annihilation. The neutrino trajectories have been obtained by using a ray-tracing algorithm, based on numerically solving the Hamilton's equations for neutrinos by reversing the proper time evolution. However, as shown by Miller et al. (2003), the picture based on the results of the on-axis calculations will probably be modified if the contribution of off-axis annihilation processes to the energy–momentum deposition is also taken into account. It is therefore crucial to extend the calculations, up to now restricted over a narrow spatial domain in the system formed by the accretion disc and compact stellar object, to the whole vicinity of the system. The information on the complete spatial distribution of the deposition rate can provide a more comprehensive insight into the scales of the electron–positron energy produced near rotating neutron and quark stars and, in turn, a more adequate description of further astrophysical processes related to the energy production mechanism via the $\nu\bar{\nu}$ pair annihilation.

Motivated by this goal, it is the purpose of the present paper to present a full three-dimensional general relativistic numerical code for the study of the electron–positron energy deposition rate from the neutrino–antineutrino annihilation process, and to obtain the basic physical parameters characterizing this process (the electron–positron energy deposition rate per unit volume and unit time) by taking into account the full general relativistic corrections. The source of the neutrinos is assumed to be the accretion disc that can be formed around neutron and quark stars (Zhang & Dai 2009). The code is used to obtain the full three-dimensional distribution of the electron–positron energy deposition rate around neutron and quark stars described by several types of equations of state.

In order to compute the electron–positron energy deposition rate, the metric outside the rotating general relativistic stars must be determined. In the present study we obtain the equilibrium configurations of the rotating neutron and quark stars by using the Rotating Neutron Star (RNS) code, as introduced in Stergioulas & Friedman (1995). The software provides the metric potentials for various types of compact rotating general relativistic objects, which can be used to obtain the electron–positron energy deposition rate on the rotation axis of rotating neutron and quark stars.

The present paper is organized as follows. In Section 2 we present the basic formalism for the calculation of the kinematic parameters (four-momenta) of the neutrino–antineutrino annihilation process, and for obtaining the electron–positron energy deposition rate. The ray-tracing code is introduced in Section 3. The equations of state of the neutron and quark stars used in the numerical simulations are presented in Section 4. The electron–positron energy deposition rates for the considered dense neutron and quark matter equations of state are obtained, for two different disc models, in Section 5. In Section 6 we consider in detail the effect of the stellar rotation on the electron–positron energy deposition rate. We discuss and conclude our results in Section 7.

2 ENERGY DEPOSITION RATE FROM $\nu\bar{\nu}$ PAIR ANNIHILATION

As a starting point in our study of the neutrino–antineutrino pair annihilation processes we consider a geometrically thin accretion disc, rotating around a compact general relativistic object. We assume that the mass energy of the disc has only a negligible effect on the stationary and axisymmetric space–time geometry. In the adapted coordinate system $x^{\mu} = (t, \phi, x^1, x^2)$, with the time-like and space-like Killing vector fields $\partial/\partial t$ and $\partial/\partial\phi$, respectively, the metric is given by

$$\mathrm{d}s^2 = c^2 g_{tt}\mathrm{d}t^2 + 2cg_{t\phi}\mathrm{d}t\mathrm{d}\phi + g_{\phi\phi}\mathrm{d}\phi^2 + g_{11}\mathrm{d}(x^1)^2 + g_{22}\mathrm{d}(x^2)^2. \quad (1)$$

The metric outside the rotating compact general relativistic stars can be described, in quasi-isotropic coordinates, as (Stergioulas, Kluzniak & Bulik 1999)

$$\mathrm{d}s^2 = -c^2 e^{\gamma+\rho}\mathrm{d}t^2 + e^{2\alpha}(\mathrm{d}\bar{r}^2 + \bar{r}^2\mathrm{d}\theta^2) + e^{\gamma-\rho}\bar{r}^2\sin^2\theta(\mathrm{d}\phi - \omega\mathrm{d}t)^2, \tag{2}$$

where the metric potentials γ, ρ, α and the angular velocity of the stellar fluid relative to the local inertial frame ω are all functions of the quasi-isotropic radial coordinate $\bar{r}$ and of the poloidal angle θ. Hence, we chose the coordinates x^1 and x^2 to be $\bar{r}$ and θ, and we introduce the metric functions α, γ, ρ and ω, respectively. Then the metric components can be written as

$$g_{tt} = -e^{\gamma+\rho} + e^{\gamma-\rho}\bar{r}^2(\omega/c)^2\sin^2\theta, \tag{3}$$

$$g_{t\phi} = e^{\gamma-\rho}(\omega/c)\bar{r}^2\sin^2\theta, \tag{4}$$

$$g_{\bar{r}\bar{r}} = e^{2\alpha}, \tag{5}$$

$$g_{\theta\theta} = \bar{r}^2 e^{2\alpha}, \tag{6}$$

$$g_{\phi\phi} = e^{\gamma-\rho}\bar{r}^2\sin^2\theta. \tag{7}$$

If the effect of the disc on the metric structure can be ignored then in the vicinity of the disc and of the central object any massless particle propagate along null geodesics, which are determined by the geometry of the rotating compact star. We also suppose that the disc is the primary source of neutrinos in the system, and we neglect any interaction between the disc and the neutrino–antineutrino radiation after their generation with a relatively low temperature ($\sim$1 MeV). The low radiation temperature reduces the scattering cross-section of the ν and $\bar{\nu}$ collision with the neutrons or quarks, which allows us to neglect energy losses in the interaction with the stellar matter. As a result, we can also assume that these particles remain in geodesic motion even in the interior of the central object. Our aim is to determine the EMDR due to the neutrino–antineutrino pair annihilations into e^-e^+ pairs near the rotating compact general relativistic object.

2.1 Energy–momentum deposition rate from neutrino–antineutrino annihilation

The four-vector of the EMDR per unit volume produced by the $\nu\bar{\nu}$ collisions at any point can be written as

$$\frac{\mathrm{d}^2\boldsymbol{P}}{\mathrm{d}t\mathrm{d}V} = \int \mathrm{d}^3\mathbf{p}_\nu \int \mathrm{d}^3\mathbf{p}_{\bar{\nu}} f_\nu(\mathbf{p}_\nu, \boldsymbol{r}) f_{\bar{\nu}}(\mathbf{p}_{\bar{\nu}}, \boldsymbol{r}) \frac{\boldsymbol{p}_\nu + \boldsymbol{p}_{\bar{\nu}}}{\varepsilon_\nu \varepsilon_{\bar{\nu}}} \{\sigma_{\nu\bar{\nu}}|\boldsymbol{v}_\nu - \boldsymbol{v}_{\bar{\nu}}|\varepsilon_\nu\varepsilon_{\bar{\nu}}\}, \tag{8}$$

where $\boldsymbol{p}_\nu = (\varepsilon_\nu/c, \mathbf{p}_\nu)$ and $\boldsymbol{p}_{\bar{\nu}} = (\varepsilon_{\bar{\nu}}/c, \mathbf{p}_{\bar{\nu}})$ are the four-momenta of the neutrinos and antineutrinos with energies ε_ν and $\varepsilon_{\bar{\nu}}$, and three-momentum components $\mathbf{p}_\nu$ and $\mathbf{p}_{\bar{\nu}}$, whereas f_ν and $f_{\bar{\nu}}$ are the number densities, and $\boldsymbol{v}_\nu$ and $\boldsymbol{v}_{\bar{\nu}}$ are the three-velocities of the colliding neutrino–antineutrino pairs, respectively (Goodman et al. 1987). The cross-section of the collision is denoted by $\sigma_{\nu\bar{\nu}}$, and in the collision frame can be calculated by using the formula

$$\begin{aligned}\sigma_{\nu\bar{\nu}} &= KG_F^2(\varepsilon_\nu\varepsilon_{\bar{\nu}}/c^2 - \mathbf{p}_\nu\cdot\mathbf{p}_{\bar{\nu}}) \\ &= -KG_F^2\,\boldsymbol{p}_\nu\cdot\boldsymbol{p}_{\bar{\nu}},\end{aligned} \tag{9}$$

where $K = (1 \pm 4\sin^2\theta_W + 8\sin^4\theta_W)/6\pi$, with $\sin^2\theta_W = 0.23$, and $G_F^2 = 5.29\times10^{-44}\,\mathrm{cm}^2\,\mathrm{MeV}^{-2}$. By applying the decompositions $\mathbf{p}_\nu = (\varepsilon_\nu/c)\boldsymbol{\Omega}_\nu$ and $\mathrm{d}^3\mathbf{p}_\nu = (\varepsilon_\nu^2/c)\mathrm{d}\varepsilon_\nu\mathrm{d}\boldsymbol{\Omega}_\nu$ with the solid angle vector $\boldsymbol{\Omega}_\nu = (\cos\psi, \sin\psi\cos\xi, \sin\psi\sin\xi)$ pointing in the direction of $\mathbf{p}_\nu$ (determined by the sky angles ψ and ξ) and by assuming that the neutrino source in the disc emits particles isotropically, the integral in equation (8) can be separated into an energy integral and an angular part.

After inserting the scalar product of the four-momenta into the expression of the cross-section $\sigma_{\nu\bar{\nu}}$, given by equation (9), and evaluating the energy integrals for fermions in the isotropic case, we obtain the deposited energy and momentum per unit volume and per unit time ($\mathrm{d}t\mathrm{d}V = \sqrt{-g}\mathrm{d}^4x$) in the form

$$\begin{aligned}\frac{\mathrm{d}^2\boldsymbol{P}}{\mathrm{d}t\mathrm{d}V} &= 2cKG_F^2\int\mathrm{d}\boldsymbol{\Omega}_\nu\int\mathrm{d}\boldsymbol{\Omega}_{\bar{\nu}}\int\mathrm{d}\varepsilon_\nu\varepsilon_\nu^3\int\mathrm{d}\varepsilon_{\bar{\nu}}\varepsilon_{\bar{\nu}}^3 f_\nu f_{\bar{\nu}}(\varepsilon_\nu\boldsymbol{\Omega}_\nu + \varepsilon_{\bar{\nu}}\boldsymbol{\Omega}_{\bar{\nu}})(1-\boldsymbol{\Omega}_\nu\cdot\boldsymbol{\Omega}_{\bar{\nu}})^2\vec{\boldsymbol{\Omega}}_\nu \\ &= \frac{21\pi^4}{4}\zeta(5)\frac{KG_F^2}{h^6c^5}\int\int k^9T_0^5(\bar{r_\nu})T_0^4(\bar{r_{\bar{\nu}}})(1-\boldsymbol{\Omega}_\nu\cdot\boldsymbol{\Omega}_{\bar{\nu}})^2\vec{\boldsymbol{\Omega}}_\nu\mathrm{d}\boldsymbol{\Omega}_\nu\mathrm{d}\boldsymbol{\Omega}_{\bar{\nu}},\end{aligned} \tag{10}$$

with the 'solid angle four-vector' $\vec{\boldsymbol{\Omega}}_\nu = (c, \boldsymbol{\Omega}_\nu)$ (Salmonson & Wilson 1999). Here $T_0(\bar{r_\nu})$ and $T_0(\bar{r_{\bar{\nu}}})$ are the temperatures of the neutrino and of the antineutrino, measured by any observer at the place of the collision, and ζ is the Riemann zeta function. The neutrino and the antineutrino temperatures generally depend on the radial coordinates $\bar{r_\nu}$ and $\bar{r_{\bar{\nu}}}$ of the points where the colliding $\nu\bar{\nu}$ pairs are emitted from the surface of the disc. With the assumption that the isotropic emission of neutrinos and antineutrinos from the accretion disc produces *Planck* blackbody spectra with the same energies for both species, only the Doppler shift of the temperature due to the disc rotation must be taken into account. For a neutrino energy ε_ν, measured on the disc, the neutrino temperature, measured at the observer's location, can be written as

$$T_0(\bar{r_\nu}) = \frac{\varepsilon_\nu}{-\boldsymbol{p}_\nu\cdot\boldsymbol{u}_d(\bar{r_\nu})}T(\bar{r_\nu}), \tag{11}$$

where $\boldsymbol{u}_d(\bar{r}_\nu)$ and $T(\bar{r}_\nu)$ are the four-velocity of the disc and the neutrino temperature at the radius $\bar{r}_\nu$ of the neutrino emission point. The four-velocity of the accretion disc under the Keplerian rotation is given by

$$\boldsymbol{u}_d = \left(u^t, 0, 0, u^\phi = u^t \Omega_{\rm K}/c\right),$$

with the time component

$$u^t = \left[-g_{tt} - 2g_{t\phi}\Omega_{\rm K}/c - g_{\phi\phi}(\Omega/c)^2\right]^{-1/2}$$

and the angular frequency $\Omega_{\rm K}$ of the Keplerian disc

$$\Omega_{\rm K} = \frac{{\rm d}\phi}{{\rm d}t} = c\frac{-g_{t\phi,\bar{r}} + \sqrt{(g_{t\phi,\bar{r}})^2 - g_{tt,\bar{r}}g_{\phi\phi,\bar{r}}}}{g_{\phi\phi,\bar{r}}}.$$

The four-velocity of an accretion disc can be computed by using the metric components (3)–(7) where the angular frequency $\Omega_{\rm K}$ takes the from

$$\Omega_{\rm K} = \frac{\left(\gamma_{,\bar{r}} - \rho_{,\bar{r}} + 2\bar{r}^{-1} + \omega^{-1}\omega_{,\bar{r}}\right)}{\gamma_{,\bar{r}} - \rho_{,\bar{r}} + 2\bar{r}^{-1}}\omega + \frac{\sqrt{\omega_{,\bar{r}}^2 + c^2 e^{2\rho}\bar{r}^{-2}(\gamma_{,\bar{r}} + \rho_{,\bar{r}})\left(\gamma_{,\bar{r}} - \rho_{,\bar{r}} + 2\bar{r}^{-1}\right)}}{\gamma_{,\bar{r}} - \rho_{,\bar{r}} + 2\bar{r}^{-1}}.$$

At given points of the $\nu\bar{\nu}$ pair emission the temperature functions $T_0(\bar{r}_\nu)$ and $T_0(\bar{r}_{\bar{\nu}})$ in equation (10) can be evaluated in the quasi-isotropic coordinate system by using the expressions of $\Omega_{\rm K}$ and u_t. Then equation (10) can be written as

$$\frac{{\rm d}^2\boldsymbol{P}}{{\rm d}t{\rm d}V} = \frac{\widetilde{\alpha}}{c}\int_0^{\pi/2}{\rm d}\psi_\nu \sin\psi_\nu \int_0^{2\pi}{\rm d}\xi_\nu z_\nu^5(\psi_\nu, \xi_\nu)\int_0^{\pi/2}{\rm d}\psi_{\bar{\nu}}\sin\psi_{\bar{\nu}}\int_0^{\pi/2}{\rm d}\xi_{\bar{\nu}} z_{\bar{\nu}}^4(\psi_{\bar{\nu}}, \xi_{\bar{\nu}}) \times [1 - \cos\psi_\nu\cos\psi_{\bar{\nu}} - \sin\psi_\nu\sin\psi_{\bar{\nu}}\cos(\xi_\nu - \xi_{\bar{\nu}})]^2\,\vec{\boldsymbol{\Omega}}_\nu(\psi_\nu, \xi_\nu), \quad (12)$$

where the cofactor of the integral depends on the neutrino temperature T, measured in the corotating frame of the accretion disc, and is given by $\widetilde{\alpha} = 1.84 \times 10^{32}(kT/10\,{\rm MeV})^9\ {\rm erg\,s^{-1}cm^{-3}}$ (Miller et al. 2003). For null geodesic originating from the accretion disc and arriving at the observer from the direction determined by the sky angles (ψ_ν, ξ_ν) the redshift factor z_ν is equal to $\varepsilon_\nu/(-\boldsymbol{p}_\nu\cdot\boldsymbol{u}_d(\psi_\nu, \xi_\nu))$. If the origin of the geodesic from the given direction is outside of the disc then z_ν is set to 0. The definition of $z_{\bar{\nu}}$ is the same as for the neutrinos, but it is calculated for the energy $\varepsilon_{\bar{\nu}}$ and the direction determined by the sky angles $(\psi_{\bar{\nu}}, \xi_{\bar{\nu}})$. From this condition it follows that the redshift factor strongly depends on the position of the observer.

2.2 Geometry of the geodesics

In order to determine the origin of the geodesics of the colliding $\nu\bar{\nu}$ pairs, we traced the null geodesics back from the observer to either the disc surface, occupying a finite area in the equatorial plane, or until they reached the coordinate radius $25r_g$ ($r_g = 2GM/c^2$, where M is the total mass of the central star). The geodesic curves passing through any fixed point in the space–time are uniquely determined by the tangent vector of the curve at that point, i.e. the four-momentum of the particle propagating along the curve. The collision angles determine the four-momentum $\boldsymbol{p}_\nu = (\varepsilon_\nu/c)\vec{\boldsymbol{\Omega}}_\nu$ of a neutrino measured in the locally Lorentzian collision frame (LLF), as can be seen in Fig. 1. The components of the four-momentum in any global coordinate system can be derived by applying a tetrad transformation of the LLF vector components to any global coordinate system at the location of the observer,

$$p^\mu = e^\mu{}_{(\nu)}p^{(\nu)}_{\rm LLF}. \quad (13)$$

For null particles, the tetrad components can be computed from the normalization condition $\boldsymbol{p}\cdot\boldsymbol{p} = 0$. In a stationary and axisymmetric space–time given by equation (1) the tetrad transforming four-vectors from the local frame to the quasi-isotropic coordinate system is given

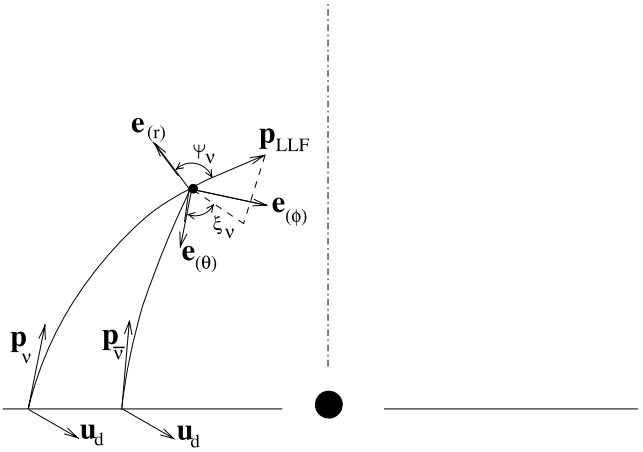

Figure 1. The four-momentum of the neutrino measured in the LLF at the position of its collision with its anti-particle.

by

$$\boldsymbol{e}_{(t)} = (-g_{tt})^{-1/2}\left(1, 0, 0, -g_{t\phi}\Delta_g^{-1/2}\right),$$

$$\boldsymbol{e}_{(r)} = g_{\bar{r}\bar{r}}^{-1/2}(0, 1, 0, 0),$$

$$\boldsymbol{e}_{(\theta)} = g_{\theta\theta}^{-1/2}(0, 0, 1, 0),$$

$$\boldsymbol{e}_{(\phi)} = (-g_{tt}/\Delta_g)^{1/2}(0, 0, 0, 1),$$

with $\Delta_g = g_{t\phi}^2 - g_{tt}g_{\phi\phi}$ (Miller et al. 2003). Inserting the metric components (3)–(7) into these equations, we obtain

$$\boldsymbol{e}_{(t)} = e^{-(\gamma+\rho)/2}(1 - F^2)^{-1/2}(1, 0, 0, F),$$

$$\boldsymbol{e}_{(r)} = e^{-\alpha}(0, 1, 0, 0),$$

$$\boldsymbol{e}_{(\theta)} = \bar{r}^{-1}e^{-\alpha}(0, 0, 1, 0),$$

$$\boldsymbol{e}_{(\phi)} = e^{\gamma/2}[(\omega/c)(1 - F^2)/F]^{1/2}(0, 0, 0, 1),$$

where we have used the short-hand notation $F = e^{-\rho}\bar{r}(\omega/c)\sin\theta$. The neutrino momentum $\mathbf{p}_\nu$ is obtained by specifying the neutrino energy ϵ_ν with the sky angles ψ_ν and ξ_ν, and applying the tetrad transformation (13). For any stationary and axisymmetric geometry its covariant components $p_t = -E/c$ and $p_\phi = L$, namely, the energy and the angular momentum of the particle propagating in the space–time, are constants of motion. (We note that E is a function of not only ε_ν but also the sky angles). Then the coordinate functions $x^\mu(\tau) = [t(\tau), \bar{r}(\tau), \theta(\tau), \phi(\tau)]$ are the dependent variables of the geodesic equations in which the constants of motions appear as parameters. Since the geodesic equation containing the proper time derivatives of $\bar{r}$ and θ is not separable in the geometry of compact general relativistic objects like neutron or quark stars, we used Hamilton's equations of motion to recast it into a more convenient form (Schnittman & Bertschinger 2004; Perez-Giz & Levin 2009): in the ray-tracing code we supplemented the coordinates of $\bar{r}$ and θ with the covariant form of their momenta $p_{\bar{r}}$ and p_θ, and used the dynamical equations for the extended set of variables. We present some details of this method in Section 3.

Following Miller et al. (2003) we placed 100 × 100 observers at equidistant points with respect to the coordinates r and θ (fixed Δr and $\Delta\theta$) in the zx plane ($\phi = 0$) between $1.25r_g < r < 6r_g$ and $0 < \theta < \pi/2$. Here r is the curvature coordinate given by the transformation (22). We calculated the EMDR four-vector at each observer in LLF by using equation (12), and we approximated the four-momentum per proper time $\mathrm{d}\boldsymbol{P}/\mathrm{d}\tau$ generated at each location as Miller et al. (2003) did: we have transformed the coordinates of the observers and the components of the EMDR four-vector into quasi-isotropic coordinates, and multiplied the four-vector by the effective spatial three-volume $\Delta\widetilde{V} = 2\pi\sqrt{g_{\bar{r}\bar{r}}g_{\phi\phi}g_{\theta\theta}}\Delta\bar{r}\Delta\theta$ assigned to each observer. Although being a coordinate-dependent quantity, $\Delta\widetilde{V} \times \mathrm{d}^2\boldsymbol{P}/\mathrm{d}t\mathrm{d}V$ provides a qualitative description of the spatial distribution of $\mathrm{d}\boldsymbol{P}/\mathrm{d}\tau$, especially far away from the central object, where the time-like curves along the tangent vector field $\partial/\partial t$ already tend to be orthogonal to the spatial slices associated with the three-volume $\Delta\widetilde{V}$.

For the plots presenting the four-vector $\Delta\widetilde{V} \times \mathrm{d}^2\mathbf{P}/\mathrm{d}t\mathrm{d}V$ in the plane of the coordinates $x = r\sin\theta$ and $z = r\cos\theta$, we have converted its components from the quasi-spheroidal coordinate system to the curvature coordinates, with the tetrad

$$\boldsymbol{e}_t = (1, 0, 0, 0),$$

$$\boldsymbol{e}_{\bar{r}} = \frac{1}{2}e^{-(\gamma-\rho)/2}[2 + (\gamma_{,\bar{r}} - \rho_{,\bar{r}})\bar{r}](0, 1, 0, 0),$$

$$\boldsymbol{e}_\theta = \frac{1}{2}e^{-(\gamma-\rho)/2}(\gamma_{,\theta} - \rho_{,\theta})(0, 0, 1, 0),$$

$$\boldsymbol{e}_\phi = (0, 0, 0, 1),$$

derived from the coordinate transformation given by equation (22) in the next section.

3 THE RAY-TRACING CODE

For massless particles propagating along null geodesics in a stationary axisymmetric space–time with metric given by equation (1), the geodesic equation of the time-derivatives $\dot{x}^1 = g^{11}p_1$ and $\dot{x}^2 = g^{22}p_2$ with respect to the proper time τ can be written as

$$g_{11}^{-1}(\dot{x}^1)^2 + g_{22}^{-1}(\dot{x}^2)^2 = V(E, L), \tag{14}$$

where the effective potential $V(E, L)$ depending on the energy E and the angular momentum L of the particle is given by

$$V(E, L) = \frac{g_{\phi\phi}(E/c)^2 + 2g_{t\phi}(E/c)L + g_{tt}L^2}{g_{t\phi}^2 - g_{tt}g_{\phi\phi}}.$$

Equation (14) is generally not a separable differential equation with respect to the coordinates x^1 and x^2. For given initial values of the coordinates at some time $\tau = \tau_0$, and for fixed constants of motion $p_t = -E/c$ and $p_\phi = L$, we can, at least numerically, integrate this equation for a null particle moving in the effective potential V. The only technical difficulty in the integration may stem from the non-separability of equation (14). However, this can be easily circumvented by introducing the momenta p_r and p_θ as dependent variables and replacing equation (14) with their canonical equations of motion (Schnittman & Bertschinger 2004; Perez-Giz & Levin 2009). Then the complete set

of the evolution equations consists of Hamilton's equations

$$\dot{x}^1 = \frac{p_1}{g_{11}}, \qquad \dot{x}^2 = \frac{p_2}{g_{22}} \tag{15}$$

$$\dot{p}_1 = \frac{1}{2}\left(\frac{g_{11,1}}{g_{11}^2}p_1^2 + \frac{g_{22,1}}{g_{22}^2}p_2^2 + V_{,1}\right), \qquad \dot{p}_2 = \frac{1}{2}\left(\frac{g_{11,2}}{g_{11}^2}p_1^2 + \frac{g_{22,2}}{g_{22}^2}p_2^2 + V_{,2}\right), \tag{16}$$

and the decoupled geodesic equations for the coordinates t and ϕ,

$$\dot{t} = \frac{1}{c}\frac{g_{\phi\phi}(E/c) + g_{t\phi}L}{g_{t\phi}^2 - g_{tt}g_{\phi\phi}}, \qquad \dot{\phi} = -\frac{g_{t\phi}(E/c) + g_{tt}L}{g_{t\phi}^2 - g_{tt}g_{\phi\phi}}. \tag{17}$$

If the space–time geometry has the form given by equation (2), with the coordinates t, ϕ, $x^1 = \bar{r}$ and $x^2 = \theta$, the system (15)–(17) can be written as

$$\dot{\bar{r}} = f^{\bar{r}}p_{\bar{r}}, \qquad \dot{\theta} = f^{\theta}p_{\theta}, \tag{18}$$

$$\dot{t} = f_1^t E/c + f_2^t L, \qquad \dot{\phi} = f_1^{\phi}E/c + f_2^{\phi}L, \tag{19}$$

$$\dot{p}_{\bar{r}} = F_1^{\bar{r}}p_{\bar{r}}^2 + F_2^{\bar{r}}p_{\theta}^2 + F_3^{\bar{r}}(E/c)^2 + F_4^{\bar{r}}(E/c)L + F_5^{\bar{r}}L^2, \tag{20}$$

$$\dot{p}_{\theta} = F_1^{\theta}p_1^2 + F_2^{\theta}p_2^2 + F_3^{\theta}(E/c)^2 + F_4^{\theta}(E/c)L + F_5^{\theta}(E/c)L^2, \tag{21}$$

with the functions

$$f^{\bar{r}} = e^{-2\alpha}, \qquad f^{\theta} = \bar{r}^{-2}e^{-2\alpha}, \qquad f_1^t = e^{-(\gamma+\rho)}/c, \qquad f_2^t = -e^{-(\gamma+\rho)}\omega/c,$$

$$f_1^{\phi} = e^{-(\gamma+\rho)}\omega, \qquad f_2^{\phi} = -e^{-(\gamma+\rho)}(\omega^2 - e^{2\rho}\bar{r}^{-2}\sin^{-2}\theta),$$

$$F_1^{\bar{r}} = e^{-2\alpha}\alpha_{,\bar{r}}, \qquad F_2^{\bar{r}} = \bar{r}^{-2}e^{-2\alpha}(\bar{r}^{-1} + \alpha_{,\bar{r}}),$$

$$F_3^{\bar{r}} = -\frac{1}{2}e^{-(\gamma+\rho)}(\gamma_{,\bar{r}} + \rho_{,\bar{r}}), \qquad F_4^{\bar{r}} = e^{-(\gamma+\rho)}[(\gamma_{,\bar{r}} + \rho_{,\bar{r}})\omega - \omega_{\bar{r}}],$$

$$F_5^{\bar{r}} = -e^{-(\gamma+\rho)}\left[\frac{1}{2}(\gamma_{,\bar{r}} + \rho_{,\bar{r}})\omega^2 - \omega\omega_{,\bar{r}} + \frac{1}{2}e^{2\rho}\left(\rho_{,\bar{r}} - \gamma_{,\bar{r}} - 2\bar{r}^{-1}\right)\bar{r}^{-2}\sin^{-2}\theta\right],$$

$$F_1^{\theta} = e^{-2\alpha}\alpha_{,\theta}, \qquad F_2^{\theta} = \bar{r}^{-2}e^{-2\alpha}\alpha_{,\theta},$$

$$F_3^{\theta} = -\frac{1}{2}e^{-(\gamma+\rho)}(\gamma_{,\theta} + \rho_{,\theta}), \qquad F_4^{\theta} = e^{-(\gamma+\rho)}[(\gamma_{,\theta} + \rho_{\theta})\omega - \omega_{,\theta}],$$

$$F_5^{\theta} = -e^{-(\gamma+\rho)}\left[\frac{1}{2}(\gamma_{,\theta} + \rho_{,\theta})\omega^2 - \omega\omega_{,\theta} + \frac{1}{2}e^{2\rho}(\rho_{,\theta} - \gamma_{,\theta} - 2\tan^{-1}\theta)\bar{r}^{-2}\sin^{-2}\theta\right],$$

depending on only the coordinates $\bar{r}$ and θ. This is a system of ordinary differential equations, with the unknown functions $\bar{r}(\tau)$, $\theta(\tau)$, $p_{\bar{r}}(\tau)$, $p_{\theta}(\tau)$, $t(\tau)$ and $\phi(\tau)$, respectively. The constants of motion E and L are considered as parameters of the system. If the parameters and the initial values of the unknown functions are given, so that the mass-shell condition $\boldsymbol{p}\cdot\boldsymbol{p} = 0$ holds (a constraint imposed on the initial data), then the system of differential equations (18)–(21) can be integrated numerically. In the ray-tracing algorithm we have applied the fourth-order adaptive Runge–Kutta method for the integration.

In order to calculate the equilibrium configurations of the rotating neutron and quark stars with different equations of state we use the RNS code, as introduced in Stergioulas & Friedman (1995), and discussed in detail in Stergioulas (2003). This code was used for the study of different models of rotating neutron stars (Nozawa et al. 1998), and for the study of the rapidly rotating strange stars (Stergioulas et al. 1999). The RNS code computes the metric functions in a quasi-spheroidal coordinate system and writes them as functions of the compactified dimensionless distance $s = \bar{r}/(\bar{r} + \bar{r}_{\rm e})$, where $\bar{r}_{\rm e}$ is the equatorial radius of the star, and the cosine of the poloidal angle. The quasi-spheroidal radial coordinate is converted into curvature radius r according to the equation

$$r = \bar{r}\exp\left\{[\gamma(\bar{r},\theta) - \rho(\bar{r},\theta)]/2\right\}, \tag{22}$$

where the latter coordinate will be used in the graphic presentation of the physical quantities calculated in the following sections.

In order to determine the metric functions α, γ, ρ and ω and their spatial derivatives in the evolution equations, we have used numerical tables generated by the RNS code with a high-resolution mesh (1001×3001) of the compactified quasi-isotropic radial coordinate $s = \bar{r}/(\bar{r} + \bar{r}_{\rm e})$, and the angular coordinate $\mu = \cos\theta$. Since the code calculates the metric functions and their derivative functions only at the two-dimensional grid points (s, μ) we applied bi-cubic interpolation to evaluate all the functions at any arbitrary point $(\bar{r}, \theta)$ between the discrete points of the numerical tables. The derivatives with respect to $\bar{r}$ and θ of the metric functions were calculated from their derivatives with respect to the grid variables s and μ.

For a given set of canonical data $[\bar{r}(\tau_0), \theta(\tau_0), p_{\bar{r}}(\tau_0), p_{\theta}(\tau_0)]$, we traced the (anti)neutrinos back from the observers in the zx plane either to the equatorial plane, where they are supposed to be produced, or to any point up to the radius $25r_g$. At the location of the observer, specified with the coordinates $[\bar{r}(\tau_0), \theta(\tau_0)]$, the momenta $p_{\bar{r}}(\tau_0)$, $p_{\theta}(\tau_0)$ together with the parameters E/c and L were calculated from equations (13). For given collision angles (ψ, ξ) and a fixed value of ε, the four-momentum measured in the LLF was obtained from the expression $\boldsymbol{p}_{\rm LLF} = (\varepsilon/c)\vec{\boldsymbol{\Omega}}$ (Miller et al. 2003). If the geodesic curve crossed the equatorial plane in the area between the inner and the outer edge of the

disc, the exact radius of the intersection point was determined from a cubic spline interpolation of the closest 3–3 data points located on the curve above and below the equatorial plane.

4 EQUATIONS OF STATE AND STELLAR MODELS

In order to obtain a consistent and realistic physical description of the rotating general relativistic neutron and quark stars, we have to adopt the equations of state for the dense neutron and quark matter, respectively. In the present study we consider the following equations of state.

(i) Akmal–Pandharipande–Ravenhall (APR) Equation of State (EOS) (Akmal, Pandharipande & Ravenhall 1998). EOS APR has been obtained by using the variational chain summation methods and the Argonne v_{18} two-nucleon interaction. Boost corrections to the two-nucleon interaction, which give the leading relativistic effect of order $(v/c)^2$, as well as three-nucleon interactions, are also included in the nuclear Hamiltonian. The density range is from 2×10^{14} to 2.6×10^{15} g cm^{-3}. The maximum mass limit in the static case for this EOS is 2.20 $M_\odot$. We join this equation of state to the composite BBP ($\epsilon/c^2 > 4.3 \times 10^{11}$ g cm^{-3}) (Baym, Bethe & Pethick 1971a), BPS ($10^4 < 4.3 \times 10^{11}$ g cm^{-3}) (Baym, Pethick & Sutherland 1971b), FMT ($\epsilon/c^2 < 10^4$ g cm^{-3}) (Feynman, Metropolis & Teller 1949) equations of state, respectively.

(ii) Douchin–Haensel (DH) EOS (Douchin & Haensel 2001). EOS DH is an equation of state of the neutron star matter, describing both the neutron star crust and the liquid core. It is based on the effective nuclear interaction SLy of the Skyrme type, which is particularly suitable for the application to the calculation of the properties of very neutron rich matter. The structure of the crust, and its EOS, is calculated in the zero temperature approximation, and under the assumption of the ground state composition. The EOS of the liquid core is calculated assuming (minimal) $npe\mu$ composition. The density range is from 3.49×10^{11} to 4.04×10^{15} g cm^{-3}. The minimum and maximum masses of the static neutron stars for this EOS are 0.094 and 2.05 $M_\odot$, respectively.

(iii) Shen–Toki–Oyamatsu–Sumiyoshi (STOS) EOS (Shen et al. 1998). The STOS equation of state of nuclear matter is obtained by using the relativistic mean field (RMF) theory with non-linear σ and ω terms in a wide density and temperature range, with various proton fractions. The EOS was specifically designed for the use of supernova simulation and for the neutron star calculations. The Thomas–Fermi approximation is used to describe inhomogeneous matter, where heavy nuclei are formed together with free nucleon gas. The temperature is mentioned for each STOS equation of state, so that, for example, STOS0 represents the STOS EOS for $T = 0$ MeV. For the proton fraction we chose the value $Y_p = 10^{-2}$ in order to avoid the negative pressure regime for low baryon mass densities.

(iv) RMF equations of state with isovector scalar mean field corresponding to the δ-meson-soft RMF and stiff RMF EOS (Kubis & Kutschera 1997). While the δ-meson mean field vanishes in symmetric nuclear matter, it can influence properties of asymmetric nuclear matter in neutron stars. The RMF contribution due to the δ-field to the nuclear symmetry energy is negative. The energy per particle of neutron matter is then larger at high densities than the one with no δ-field included. Also, the proton fraction of β-stable matter increases. Splitting of proton and neutron effective masses due to the δ-field can affect transport properties of neutron star matter. The equations of state can be parametrized by the coupling parameters $C_\sigma^2 = g_\sigma^2/m_\sigma^2$, $C_\omega^2 = g_\omega^2/m_\omega^2$, $\bar{b} = b/g_\sigma^3$ and $\bar{c} = c/g_\sigma^4$, where m_σ and m_ω are the masses of the respective mesons, and b and c are the coefficients in the potential energy $U(\sigma)$ of the σ-field. The soft RMF EOS is parametrized by $C_\sigma^2 = 1.582$ fm^2, $C_\omega^2 = 1.019$ fm^2, $\bar{b} = -0.7188$ and $\bar{c} = 6.563$, while the stiff RMF EOS is parametrized by $C_\sigma^2 = 11.25$ fm^2, $C_\omega^2 = 6.483$ fm^2, $\bar{b} = 0.003825$ and $\bar{c} = 3.5 \times 10^{-6}$, respectively.

(v) Baldo–Bombaci–Burgio (BBB) EOS (Baldo, Bombaci & Burgio 1997). The BBB EOS is an EOS for asymmetric nuclear matter, derived from the Brueckner–Bethe–Goldstone many-body theory with explicit three-body forces. Two EOSs are obtained, one corresponding to the Argonne AV14 (BBBAV14), and the other to the Paris two-body nuclear force (BBBParis), implemented by the Urbana model for the three-body force. The maximum static mass configurations are $M_{\max} = 1.8\,M_\odot$ and $M_{\max} = 1.94\,M_\odot$ when the AV14 and Paris interactions are used, respectively. The onset of direct Urca processes occurs at densities $n \geq 0.65$ fm^{-3} for the AV14 potential and $n \geq 0.54$ fm^{-3} for the Paris potential. The comparison with other microscopic models for the EOS shows noticeable differences. The density range is from 1.35×10^{14} g cm^{-3} to 3.507×10^{15} g cm^{-3}.

(vi) Bag model equation of state for quark matter (Q) EOS (Itoh 1970; Bodmer 1971; Witten 1984; Cheng, Dai & Lu 1998). For the description of the quark matter we adopt first a simple phenomenological description, based on the MIT bag model equation of state, in which the pressure p is related to the energy density ρ by

$$p = \frac{1}{3}(\rho - 4B)c^2, \tag{23}$$

where B is the difference between the energy density of the perturbative and non-perturbative Quantum Chromodynamics (QCD) vacuum (the bag constant), with the value $4B = 4.2 \times 10^{14}$ g cm^{-3}.

(vii) It is generally agreed today that the colour–flavour-locked (CFL) state is likely to be the ground state of matter, at least for asymptotic densities, and even if the quark masses are unequal (Alford, Rajagopal & Wilczek 1999; Rapp et al. 2000; Horvath & Lugones 2004; Alford et al. 2008). Moreover, the equal number of flavours is enforced by symmetry, and electrons are absent, since the mixture is automatically neutral. By assuming that the mass m_s of the s quark is not large as compared to the chemical potential μ, the thermodynamical potential of the quark matter in CFL phase can be approximated as (Lugones & Horvath 2002)

$$\Omega_{\rm CFL} = -\frac{3\mu^4}{4\pi^2} + \frac{3m_s^2}{4\pi^2} - \frac{1 - 12\ln(m_s/2\mu)}{32\pi^2}m_s^4 - \frac{3}{\pi^2}\Delta^2\mu^2 + B, \tag{24}$$

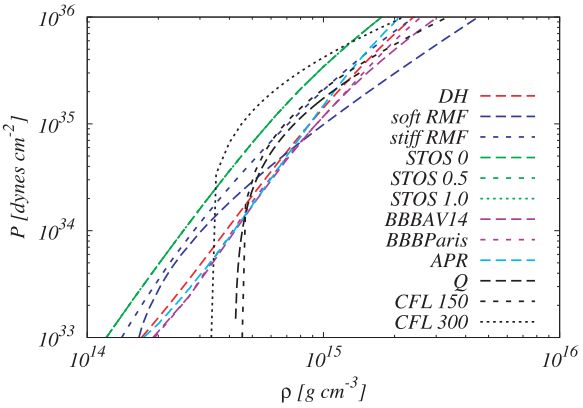

Figure 2. Pressure as a function of density (in a logarithmic scale) for the equations of state DH, RMF soft, RMF stiff, STOS 0. STOS 0.5, STOS 1, BBBAV14, BBBParis, APR, Q, CFL150 and CFL300, respectively.

where Δ is the gap energy. With the use of this expression the pressure P of the quark matter in the CFL phase can be obtained as an explicit function of the energy density ε in the form (Lugones & Horvath 2002)

$$P = \frac{1}{3}(\varepsilon - 4B) + \frac{2\Delta^2\delta^2}{\pi^2} - \frac{m_s^2\delta^2}{2\pi^2}, \tag{25}$$

where

$$\delta^2 = -\alpha + \sqrt{\alpha^2 + \frac{4}{9}\pi^2(\varepsilon - B)}, \tag{26}$$

and $\alpha = -m_s^2/6 + 2\Delta^2/3$. In the following the value of the gap energy Δ considered in each case will be also mentioned for the CFL equation of state, so that, for example, CFL200 represents the CFL EOS with $\Delta = 200$. For the bag constant B we adopt the value $4B = 4.2 \times 10^{14}\,\mathrm{g\,cm^{-3}}$, while for the mass of the strange quark we take the value $m_s = 150$ MeV.

The pressure–density relation for the considered equations of state is presented in Fig. 2.

5 DEPOSITION RATE NEAR ROTATING COMPACT STARS

In the present section we present the spatial distribution of the EMDR due to the $\nu\bar{\nu}$ pair annihilation in the vicinity of rotating neutron and quark stars with the EOS presented in Section 4. We consider two types of geometrically thin accretion disc models with a neutrino–antineutrino radiation, as considered in Asano & Fukuyama (2001) and Miller et al. (2003). The first model is an accretion disc in an isothermal state, where the effective temperature is set to be a constant $T(3r_g)$ over the entire surface of the disc. The constant $T(3r_g)$ is the temperature measured at $r = 3r_g$ in the frame of reference corotating with the disc. Then the neutrino temperature T_0 at the place of the collision, given by equation (11), has only an implicit dependence on the radial coordinate, measured along the disc, via the gravitational redshift and the Lorentz boost, respectively.

The second type of the disc models uses a thermodynamical equilibrium approximation for the disc. Therefore, the temperature is inversely proportional to the disc radius. Following Asano & Fukuyama (2001) and Miller et al. (2003), we assume that the radial distribution of the temperature profile is given by the equation $T(r) = T(3r_g)3r_g/r$. We also set the position of the outer edge of the accretion disc to the radius $5r_g$, which is the same as the one used by Miller et al. (2003). The inner edge of the disc is determined either by the marginally stable orbit r_{ms} of the gravitational potential, or, if it is less than the equatorial radius R_{e} of the central star, by the equatorial radius itself. The latter is defined to be the radius where the pressure of the stellar matter drops to zero in the equatorial plane. Since the configurations of the stellar models considered here do not produce stars compact enough to form a neutrino-sphere trapping the (anti)neutrinos, the entire surface of the accretion disc is considered as a neutrino–antineutrino source (Kovács et al. 2010).

We used equation (12) to calculate the EMDR due to the annihilation of the colliding neutrinos and antineutrinos, emitted by the thin accretion disc. The angular integral is computed over 250×250 grid points, covering the celestial sphere, and therefore we traced more then 60 000 geodesics back from the location of each observer of the 10^4 to the disc, or to the sphere at $25r_g$.

5.1 Constant temperature discs

5.1.1 Local energy deposition rates

In Figs 3 and 4 we present the EMDR derived at 10^4 observers in the zx plane above the accretion disc for the rotating neutron and quark star models with the same total mass M and angular frequency Ω, when the neutrino temperature of the disc is set to the constant $T(3r_g)$. As in Kovács et al. (2010, 2011), we consider the configurations for $M = 1.8\,\mathrm{M}_\odot$ and $\Omega = 5000\,\mathrm{s}^{-1}$ for each EOS. The physical parameters for these stellar models are presented in Table A1 (Appendix A). Since for the stellar models shown in the table the spin parameter, defined by

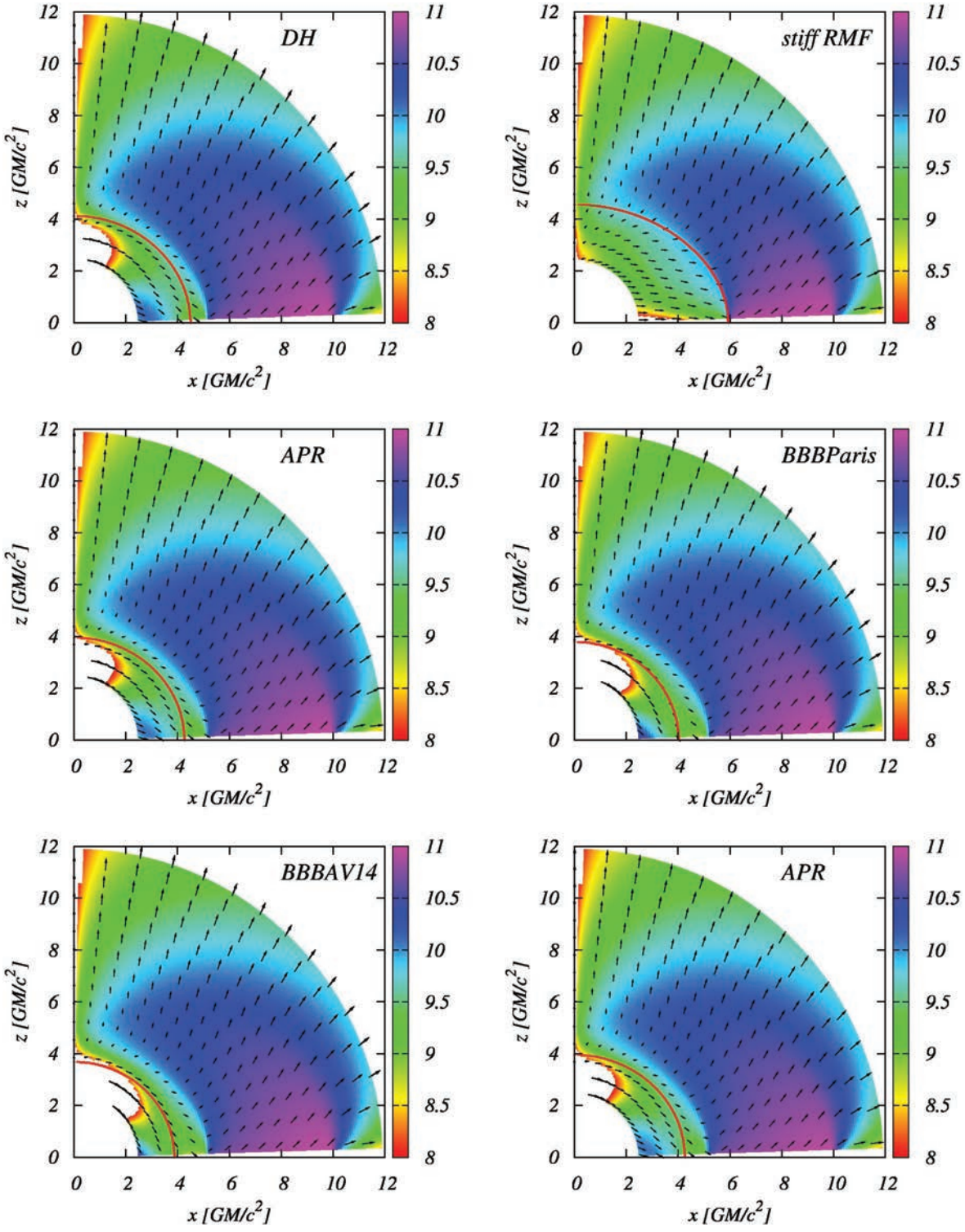

Figure 3. The spatial distribution of the EMDR four-vector $\mathrm{d}\boldsymbol{P}/\mathrm{d}\tau$ in the vicinity of a geometrically thin isothermal accretion disc, approximated by $\Delta V \times \mathrm{d}^2\boldsymbol{P}/\mathrm{d}t\mathrm{d}V$, for different models of a rotating compact neutron star, with the DH, stiff RMF, STOS0, BBBParis, BBBAV14 and APR equations of state. The total stellar mass and the angular frequency Ω are $1.8\,\mathrm{M}_{\odot}$ and $5000\,\mathrm{s}^{-1}$, respectively. The neutrino temperature of the disc is set to 1 MeV, and its outer edge is located at $5r_g$. The colour plots present the time component of the EMDR four-vector in a logarithmic scale, normalized with $\widetilde{\alpha}$, whereas the arrows indicate the projection of its spatial component (normalized with the time component) on to the *zx* plane. The red curve represents the stellar surface.

$a_* = J/M^2$ (where J is the angular momentum of the stars), has a variation between the values ∼0.3 and ∼0.8, we can compare the distribution of the annihilation rate four-vector in Figs 3 and 4 with the one calculated for Kerr black holes with similar spin. The comparison of our result with the pictorial representation of the EMDR derived for Kerr black holes in Miller et al. (2003) shows that the $\nu\bar{\nu}$ pair annihilation has very similar features for both compact stellar objects and black holes.

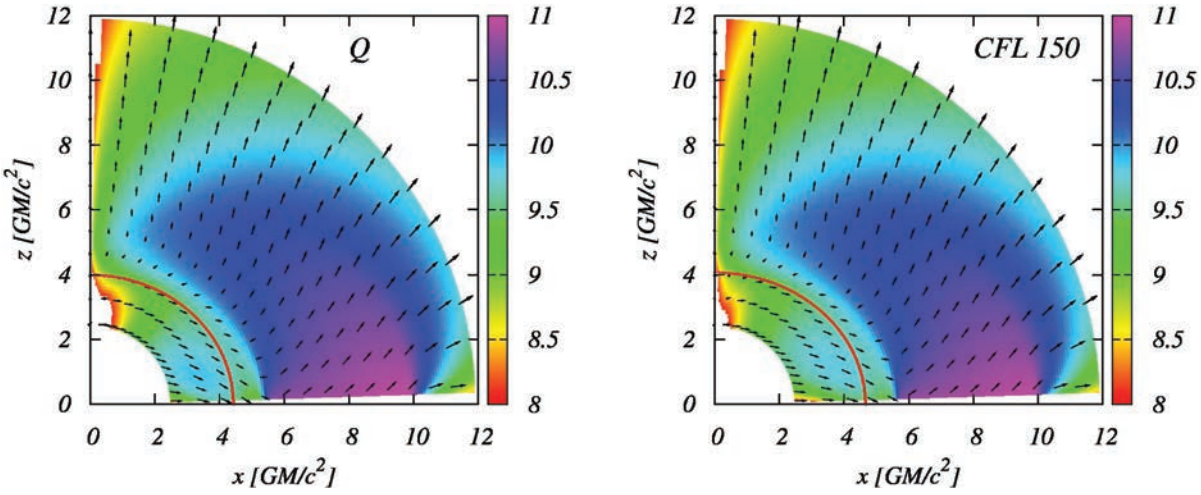

Figure 4. The same plot as in Fig. 3 but for the quark star models with Q and CFL150 type EOSs.

The colour plots representing the deposition rate four-vector near the rotating neutron and quark stars are similar to the EDMR distribution close to a rotating black hole with $a_* = 0.5$. As expected for any rotating accretion disc in a stationary and axisymmetric configuration, the intensity of the energy–momentum deposition is maximal above the disc surface and drops rapidly for positions located far from the equatorial plane. There is a considerable fall in the intensity at the disc edges but it is somewhat less steep towards the rotational axis. The three-momentum vectors of the EMDR point outwards and their magnitudes are maximal in the vicinity of the disc. Their tilt is in the direction of the disc rotation. Similar plots can be found in Birkl et al. (2007), where the EMDR distribution near the black holes was determined for different kinds of neutrino tori and disc models under the assumption of non-isotropic neutrino–antineutrino scattering. Our results are also consistent with the previous works presenting the EMDR calculations along the rotational axis and the equatorial plane of the same neutron and quark star models (Kovács et al. 2010, 2011).

Comparing the different stellar models to each other, we see that the energy–momentum deposition near the disc surface attains the highest values in the case of the stars with DH, BBBParis, BBBAV14 and APR type EOSs, respectively. The quark star models and the neutron stars with stiff RMF EOS produce somewhat less EMDR from neutrino–antineutrino annihilation, and the stellar model with STOS0 type EOS is by far the less efficient in producing energy-momentum from the colliding $\nu\bar{\nu}$ pairs. As stated in the previous works (Asano & Fukuyama 2001; Miller et al. 2003), this difference in the efficiency is mainly due to the variation of the surface area of the accretion disc. The plots demonstrate that the inner edge of the disc around neutron stars being the most effective in energy–momentum generation is located at the marginally stable orbit with the radius of $\leq 2.5r_g$, whereas the stellar surface obtained for the model with the STOS0 type EOS pushes the inner disc edge almost up to $4r_g$.

5.1.2 Global integrated deposition rates for a distant observer

In order to determine the total EMDR for a distant observer we adopt the method used by Miller et al. (2003), in which they integrated the four-vectors $\Delta\widetilde{V} \times \mathrm{d}^2\boldsymbol{P}/\mathrm{d}t\mathrm{d}V$ from the observers along their geodesics until the constant surface at $r = 25r_g$ is reached. The polar angle θ at which the four-vector hit the surface was binned into 20 bins between 0 and $\pi/2$. The values of the time-like component of the EMDR four-vector were summed up in each bin, providing the angular distribution of $\mathrm{d}^2P^t/\mathrm{d}t\mathrm{d}\Omega$ at $r = 25r_g$. The result is displayed in Fig. 5, where we plotted $\mathrm{d}^2P^t/\mathrm{d}t\mathrm{d}\Omega|_{25r_g}$ as a function of θ for each system shown in Figs 3 and 4. In the plot the integrated energy deposition rate is always concentrated along a cone of opening angle $\pi/4$, which is due to the tilt of the spatial component of the EMDR four-vector near the disc surface. Since the EMDR vector field has a similar distribution in the vicinity of the disc for each stellar model, the position of the opening angle is rather insensitive to the EOS type and it is essentially the same as the one obtained for black holes in Miller et al. (2003). However, the maximum of the peak at the cone strongly depends on the EOS type: the highest values for the deposited energy are produced for the neutron stars with APR, DH, BBBParis and BBBAV14 type EOSs, respectively. The quark stars, together with the stiff RMF-type neutron star, generate somewhat smaller peaks for the EMDR, and the energy deposition along the cone is considerably less for the stellar model with STOS0-type EOS than for the other models. Comparing the normalized values of the total EMDR in Fig. 5 with the results derived for slowly rotating Kerr black holes in Miller et al. (2003), we find that the maxima for the stellar models are roughly 10 times smaller than the ones derived for the black holes. This may be the consequence of the singularity in the numerical tables of the metric functions and their derivatives at the rotational axis, which we used in the integration of the geodesic equations. When we integrate from the observers located in the *zx* plane out to $25r_g$ many geodesic curves pass through a region close to the rotational axis because of the tilt in the direction of the EMDR four-vectors. The bi-cubic interpolation will fail in the cases where one of the grid points used by the interpolation routine coincide with the coordinate singularity. As a result, we inevitably lose the contribution of 2–3000 geodesics to the EMDR integrated over 10 000 observers (even if we use numerical tables with high angular resolution). Summing up the time components of the EMDR four-vectors tangent to the

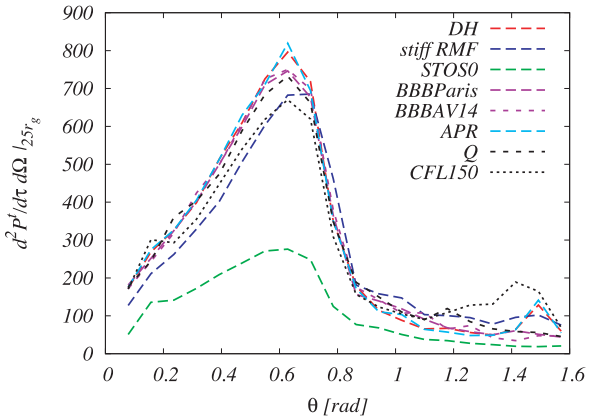

Figure 5. The deposited energy per solid angle binned as a function of the poloidal angle θ at $r = 25r_g$ for an isothermal accretion disc rotating around a compact star with the configurations shown in Figs 3 and 4. All the values are normalized with $\widetilde{\alpha}M^3$.

lost geodesics indicates that we may underestimate the total EMDR at least by 10–25 per cent. Since the contribution from lost geodesics is concentrated over the area of the cone, these numbers are high enough to reduce the peak of the deposited energy to a great extent. However, this uncertainty will not change the results of our qualitative analysis in which we have shown that the energy and momentum deposition near rotating neutron and quark stars exhibit similar features to those of the energy and momentum deposition near the Kerr black holes. For a fixed total mass M and angular frequency Ω of the central body, the nature of the EOS has an important effect both on the stellar radius and on the position of the inner edge of the accretion disc, which can, in turn, modify the integrated energy deposition rate in the vicinity of the rotating compact star. Comparing the maxima of the EMDRs calculated for the stellar models with APR and DH type EOS with those derived for the neutron stars with stiff RMF EOS and quark stars with CFL150-type EOS, respectively, we see that the peaks of the first group are about 30 per cent higher than those of the second one. The value of the total EMDR obtained for the neutron star with STOS0-type EOS is at least a factor of 3 less at the peak than the maximal values of the energy deposition rate derived in the case of the first group.

5.2 Discs in thermodynamic equilibrium

The same analysis can be applied to the accretion disc models with the thermodynamical equilibrium approximation. For the same configurations of the stellar models, the effective potential around the rotating compact stars remains the same. Then, the geometrical properties of the neutrino–antineutrino source, and the trajectories of the emitted null particles, will not change either, and the only difference is the temperature gradient of the disc, which decreases the $\nu\bar{\nu}$ energy for higher radii of the disc. Since the inner edges of the disc are located at different radii for the different stellar models, we normalize the temperature profile with $T(3r_g)$ (the temperature measured at $3r_g$) for all the models, in order to provide a neutrino–antineutrino source with more or less the same properties in each case (Asano & Fukuyama 2001; Miller et al. 2003). This normalization results in an enhancement in the disc temperature at the radii less than $3r_g$ in comparison with the constant disc temperature. The position of the inner disc edge determines this enhancement, i.e. the maximal temperature in the innermost region of the disc.

5.2.1 Local energy deposition rates

In Figs 6 and 7, we plotted the same configurations as in Figs 3 and 4 for the accretion disc with temperature gradient. The plots display the general reduction of the EMDR almost over the entire surface of the disc for all the stellar models. Only the area close to the inner disc edge can produce an amount of the EMDR comparable with the one of the isothermal disc model. The energy–momentum deposition process has characteristics similar to those found in the calculations applying the isothermal disc. The hotspot of the intensive energy–momentum deposition due to $\nu\bar{\nu}$ annihilation over the innermost region of the disc is still present in the case of the neutron star models with DH, BBBParis, BBBAV14 and APR type EOSs. The magnitude of the EMDR in that region is already smaller for the quark stars, and it is 10 times less for the stellar model with stiff RMF-type EOS. The intensity maximum near the neutron star with STOS0-type EOS is at least two order of magnitude less than the maxima in the hotspot for the stellar models depositing energy and momentum in the most efficient way.

5.2.2 Global integrated deposition rates for a distant observer

In Fig. 8, we present the angular distribution of the total EMDR integrated out to $25r_g$ for the accretion disc model in thermodynamical equilibrium. Compared with the isothermal case, there is still a relatively large component of the EMDR propagating from the innermost region of the disc to outwards. Nevertheless, the opening angle is slightly larger than $\pi/4$, and the distribution is also broader around the cone. This slight shift and the broadening of the peak of the total EMDR generated over a disc with the r^{-1} temperature profile were found in the vicinity of the rotating black holes as well (Miller et al. 2003). Comparing the distribution of the spatial component of the EMDR four-vector

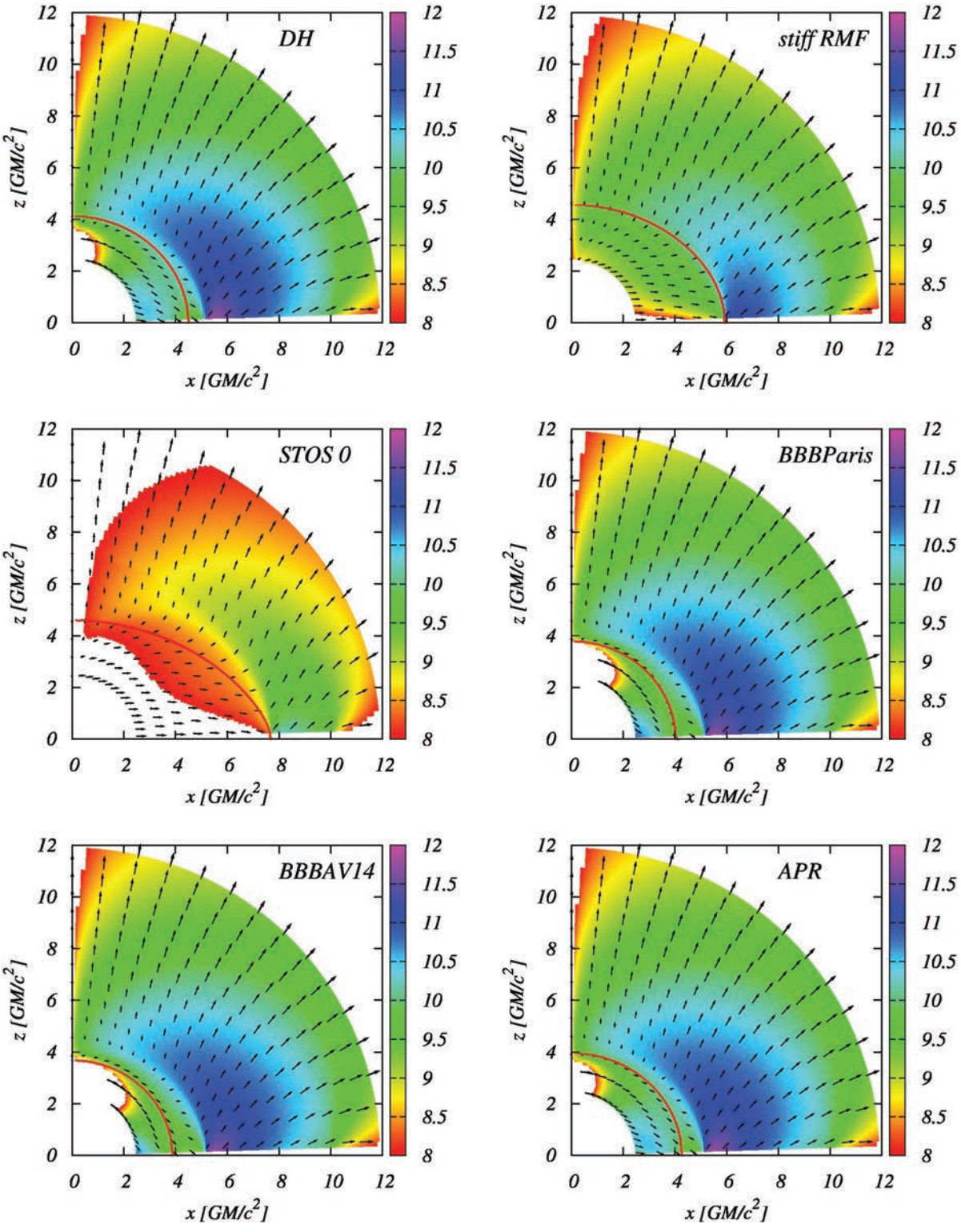

Figure 6. The same plot as in Fig. 3 but for accretion disc with temperature gradient.

close to the disc with the one close to the isothermal discs we can see that its average tilt is somewhat higher in the case of the discs in thermodynamical equilibrium, i.e. the momentum deposition rate vectors point in the directions closer to the equatorial plane. As a result, the opening angles of the surface along which the EMDR concentrates have a variation between $\pi/4$ and $\pi/3$ depending on the position of the inner edge of the accretion disc. The differences in the average tilt of the spatial component of the EMDR four-vector are enhanced by its temperature sensitivity in the innermost region of the accretion disc with $1/r$ temperature profile. Then, average tilt close to the innermost disc surface results in wider opening angles and broader angular distribution around the stiff RMF type neutron star and the quark stars

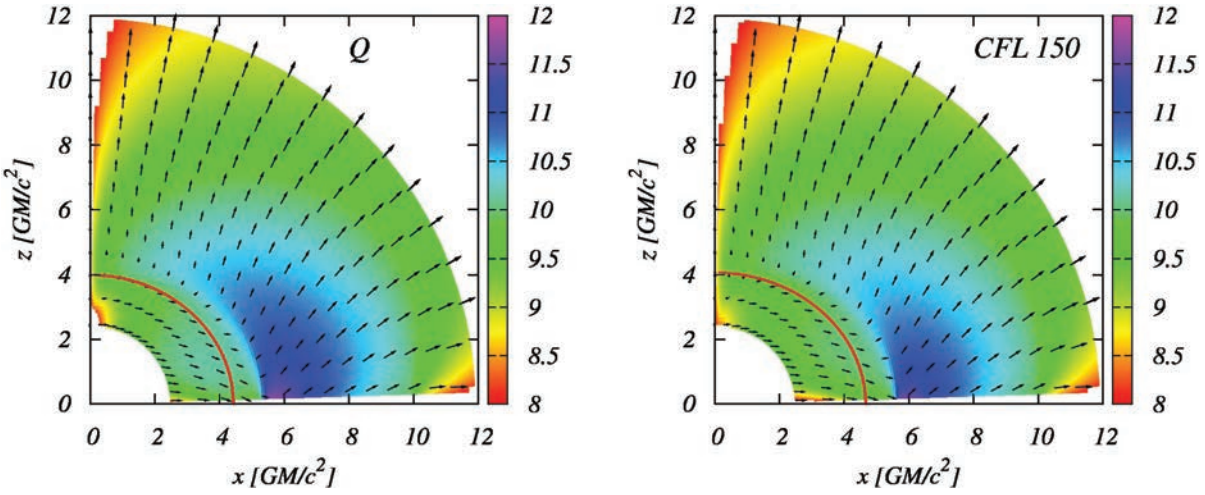

Figure 7. The same plot as in Fig. 4 but for accretion disc with temperature gradient.

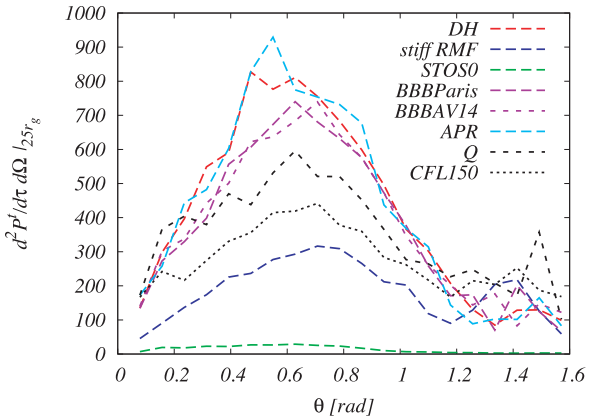

Figure 8. The same plot as in Fig. 5 but for accretion disc with temperature gradient.

whereas the position of the integrated EMDR maxima does not change much for the other stellar configurations, compared with the case of the isothermal disc. The STOS0 model with the extremely large stellar radius produces much less EMDR than the other stellar models do since the inner edge of the disc is already in a relatively cool region of the $1/r$ temperature profile. Similarly to the plots showing the spatial distribution of the EMDR, the enhancement in the deposition rate is the greatest for the neutron star models with APR, DH, BBBParis and BBBAV14 type EOSs. The quark stars are found to be less effective in the energy and momentum generation from neutrino–antineutrino annihilation, and the neutron stars with stiff RMF and SOTS0 type EOS exhibit very poor properties in this respect.

6 DEPENDENCE OF THE DEPOSITION RATE ON THE SPEED OF STELLAR ROTATION

Another way to see the effects of the variation of the disc surface area on the deposition rate is to examine the stellar models with the same stellar mass and EOS, but with different rotation velocities. As stated in Miller et al. (2003), the EMDR near a Kerr black hole has a strong dependence on the specific angular momentum of the central object. A similar dependence is expected for stellar objects too, but the situation here is more complicated even in the absence of the event horizon or, if the star is not compact enough, of a neutrino capturing region. On one hand the radius of the marginally stable orbit in the space–time of a compact star decreases with the increasing spin parameter of the body, and on the other hand the equatorial radius of the stellar surface increases as the shape of the rapidly rotating star becomes more oblate. The former effect increases the radiant area of the accretion disc, while the latter one imposes an upper boundary on it, by fixing the minimal radius at which the inner edge of the disc can be located. For black holes the area of the effective source of the $\nu\bar{\nu}$ radiation is proportional to the spin parameter, and a rapidly rotating black hole can enhance the energy–momentum deposition in its vicinity from neutrino–antineutrino annihilation (Asano & Fukuyama 2001; Miller et al. 2003). In Kovács et al. (2010, 2011) it was shown that this relation between the EDMR and a_* will break down in the case of some stellar models, where the surface of the strongly deformed star in the equatorial plane not only prevents the radiant area of the disc from the further increase, but also reduces this area by forcing the inner edge of the disc to locate at higher and higher radii. Although the higher spin indeed enhances the deposition rate even for the rapidly rotating stars with DH, BBBParis, BBBAV14 and APR type EOSs, the stiff RMF and the STOS0 models, together with the quark stars, do not follow this relation. At high rotational frequency the EMDR for the latter stellar models becomes inversely proportional to the spin parameter of the star.

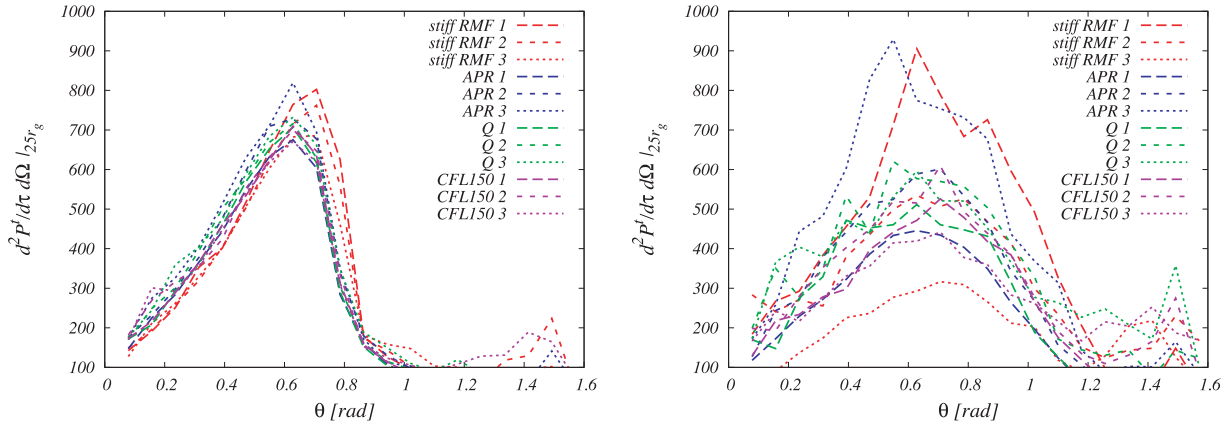

Figure 9. The deposited energy per solid angle binned as a function of the poloidal angle θ at $r = 25r_g$ for an isothermal accretion disc (right-hand side plot), and with a disc in thermodynamical equilibrium approximation (left-hand side plot) for different neutron and quark star models, rotating with different angular velocities. Ω is set to $3000\,\mathrm{s}^{-1}$ (1), $4000\,\mathrm{s}^{-1}$ (2) and $5000\,\mathrm{s}^{-1}$ (3).

This phenomenon is shown in Fig. 9, where we present the total EMDR for two neutron stars with the APR and the stiff RMF EOSs, and for two quark star models, with fixed total mass, but different angular velocities. The physical parameters of each stellar configuration with lower angular velocity than $5000\,\mathrm{s}^{-1}$ are shown in Table A2. While the stellar model with the APR-type EOS preserves the proportionality between the spin of the stellar body and the integrated EMDR up to $\Omega = 5000\,\mathrm{s}^{-1}$ (for which $a_* = 0.35$), the neutron star with stiff RMS-type EOS produces less EMDR at this angular frequency ($a_* = 0.63$) than it does for slower rotation. The quark stars also exhibit the inverted relation between a_* and the total EMDR, though to a lesser extent. The plots for the stellar models with Q and CFL150 type EOSs show that the energy–momentum deposition is not so effective at the rotational speed of $5000\,\mathrm{s}^{-1}$ ($a_* = 0.41$ and $a_* = 0.47$) as it is at lower velocities.

Considering the spin parameter in these examples, it is obvious that the proportionality between a_* and the EMDR is valid only for the domain of relatively low spin values ($a_* \leq 0.4$), and the efficiency of the energy–momentum deposition starts to decrease for higher spins, where the radiant area of the accretion disc is shrunk by the expanding stellar surface. The only difference between the stellar model with APR-type EOS and the one with stiff RMF-type EOS is the range of the rotational frequency, where they gain higher angular momentum for a fixed total mass. The former has a relatively low spin for $\Omega = 5000\,\mathrm{s}^{-1}$, while the latter reaches almost a two times higher spin value at this angular velocity. If we fix the total mass of the neutron star with APR-type EOS, and increase its rotational frequency further, we can see that the oblate spheroidal shape of the stellar object also reduces the area of its accretion disc, as the stiff RMF-type model does at lower angular velocities. For EMDR due to the annihilation of $\nu\bar{\nu}$ pairs emitted from a thin accretion disc rotating around a compact star, the most efficient configurations are those in which the central body has a moderate spin ($a_* \leq 0.4$). In this domain a_* is high enough to produce more rotational energy, which is converted into the disc radiation, but at the same time it is still low enough to prevent the stellar surface from occupying a location where it would reduce the effective radiant area of the disc (Kovács et al. 2010, 2011).

7 DISCUSSIONS AND FINAL REMARKS

Neutrino-cooled accretion discs around stellar mass black holes or neutron stars are plausible candidates for the central engine of GRBs (Zhang & Dai 2009). A phase transition during a supernova explosion can induce stellar collapse and result in large amplitude stellar oscillations (Chan et al. 2009; Cheng et al. 2009). Extremely intense pulsating neutrino fluxes, with submillisecond period and with neutrino energy greater than 30 MeV, can be emitted because the oscillations of the temperature and density are out of phase by almost 180°. Since the energy and density of neutrinos at the peaks of the pulsating fluxes are much higher than the non-oscillating case, the electron/positron pair creation rate can be enhanced significantly. Some mass layers on the stellar surface can be ejected by absorbing energy of neutrinos and pairs. These ejecta can be further accelerated to relativistic speeds by absorbing electron/positron pairs, created by the neutrino and antineutrino annihilation outside the stellar surface.

In the present paper, we have considered EMDR from the neutrino–antineutrino annihilation process around rotating neutron and quark stars. To obtain the deposition rate we have developed a full general relativistic ray-tracing algorithm. The EMDR has been calculated numerically for several equations of state of the neutron matter, and for two types of quark stars, respectively. All the general relativistic correction factors, related to this process, can be derived from the metric of the central compact object. Due to the differences in the space–time structure, the quark stars present some important differences with respect to the EMDR, as compared to the neutron stars. As a general result, we have found that there is a general correlation between the EMDR and the spin parameter of the star. There is also a strong dependence between the temperature profile of the disc and the EMDR, and at high rotational velocities the EMDR is much smaller for the model with $T \propto r^{-1}$ than the one calculated for the isothermal discs.

In our study we have neglected the possible effects of the stellar magnetic field on the external geometry of the space–time around the compact general relativistic effects, as well as on the motion of the neutrinos. Generally, we assume that the magnetic energy of the disc, $B^2/8\pi$ is much smaller than the $\rho V_{\mathrm{K}}^2/2$, the kinetic energy density of the disc, $B^2/8\pi << \rho V_{\mathrm{K}}^2/2$, where V_{K} is the Keplerian velocity. Hence

we neglect the possible influence of the magnetic field on the temperature profile of the disc. The neutrino emission rate is strongly dependent on the temperature. In the standard models of GRBs it is assumed that the central object is surrounded by a degenerate accretion disc, which allows super-Eddington accretion rates, of the order of one solar mass per second (Zhang 2007). If the central compact object is a neutron or a quark star, such super-Eddington accretion rates can maintain the compact object at very high temperatures, thus allowing very high neutrino luminosities, as well as a high rate of electron–positron pair production. The neutrino temperature can be estimated by assuming that the accretion power $\eta\dot{M}c^2$, where η is the efficiency of the energy conversion and $\dot{M}$ is the accretion rate, is equal to the radiation power $4\pi R^2\sigma T_\nu^4$, which gives the temperature as $T_\nu = (\eta\dot{M}c^2/4\pi R^2\sigma)^{1/4}$. By taking $\eta = 0.1$, $R = 10^6$ cm and an accretion rate of $\dot{M} = 1\,\mathrm{M}_\odot/10$ s, we obtain $T_\nu = 7.14 \times 10^{10}$K, a temperature which is of the order of MeV. Therefore, if the accretion disc is fed at a high rate, like, for example, by the fallback material after a supernova explosion, a high neutrino–antineutrino emission rate can be maintained, and this could explain some of the basic properties of the GRB phenomenon. In our study, we have tried to give a high numerical accuracy description of these important astrophysical processes. As shown in Miller et al. (2003) and Birkl et al. (2007), respectively, the error in the calculation of the energy deposition rate is less than 5 per cent if the number of the points over the full celestial sphere used in the integration is of the order of 10^4. Since we have integrated the EMDR over more than 6×10^4 points, we expect that the minimal error produced by our method is of the order of 5 *per cent*. The loss of the geodesics due to the coordinate singularity along the rotational axis may increase this error up to 15 per cent, and even to 30 per cent in some cases which makes our quantitative analysis somewhat uncertain in the region surrounding the compact objects. Nevertheless, in the comparison of various compact star models the effects due to the differences in the inner cut-off radii of the accretion discs dominate over those caused by the local variation of effective potential, especially close to the rotational axis. We therefore do not expect that the resolution of the uncertainty would modify the qualitative picture to a great extent which has been presented here on the energy generation mechanism from $\nu\bar{\nu}$ pair annihilation near rotating neutron and quark stars.

ACKNOWLEDGMENTS

We would like to thank to the referee, Dr Maximilian Ruffert, for his careful reading of the manuscript, and for comments and suggestions that helped us to significantly improve our paper. ZK is indebted to Dr Reiner Birkl for valuable discussions. The work of ZK was supported by the RGC General Research Fund grants HKU 701109P and 400910, respectively. TH was supported by a GRF grant of the Government of the Hong Kong SAR.

REFERENCES

Akmal A., Pandharipande V. R., Ravenhall D. G., 1998, Phys. Rev. C, 58, 1804
Alford M. G., Rajagopal K., Wilczek F., 1999, Nucl. Phys. B, 537, 433
Alford M. G., Schmitt A., Rajagopal K., Schaefer T., 2008, Rev. Mod. Phys., 80, 1455
Asano K., Fukuyama T., 2000, ApJ, 531, 949
Asano K., Fukuyama T., 2001, ApJ, 546, 1019
Asano K., Iwamoto S., 2002, ApJ, 581, 381
Baldo M., Bombaci I., Burgio G. F., 1997, A&A, 328, 274
Baym G., Bethe H. A., Pethick C. J., 1971a, Nucl. Phys. A, 175, 225
Baym G., Pethick C. J., Sutherland P., 1971b, ApJ, 170, 299
Bhattacharyya A., Ghosh S. K., Mallick R., Raha S., 2009, preprint (arXiv:0905.3605)
Birkl R., Aloy M. A., Janka H.-Th., Muller E., 2007, A&A, 463, 51
Bodmer A. R., 1971, Phys. Rev. D, 4, 1601
Chan T. C., Cheng K. S., Harko T., Lau H. K., Lin L. M., Suen W. M., Tian X. L., 2009, ApJ, 695, 732
Cheng K. S., Dai Z. G., Lu T., 1998, Int. J. Mod. Phys. D, 7, 139
Cheng K. S., Harko T., Huang Y. F., Lin L. M., Suen W. M., Tian X. L., 2009, J. Cosmol. Astropart. Phys., 09, 007
Cooperstein J., van den Horn L. J., Baron E. A., 1986, ApJ, 309, 653
Cooperstein J., van den Horn L. J., Baron E. A., 1987, ApJ, 321, L129
Douchin F., Haensel P., 2001, A&A, 380, 151
Feynman R. P., Metropolis N., Teller E., 1949, Phys. Rev., 75, 1561
Goodman J., Dar A., Nussinov S., 1986, ApJ, 314, L7
Harikae S., Kotake K., Takiwaki T., Sekiguchi Y. I., 2010a, ApJ, 720, 614
Harikae S., Kotake K., Takiwaki T., 2010b, ApJ, 713, 304
Horvath J. E., Lugones G., 2004, A&A, 422, L1
Itoh N., 1970, Prog. Theor. Phys., 44, 291
Kovács Z., Cheng K. S., Harko T., 2010, MNRAS, 402, 1714
Kovács Z., Cheng K. S., Harko T., 2011, MNRAS, 411, 1503
Kubis S., Kutschera M., 1997, Phys. Lett. B, 399, 191
Liu T., Liang E.-W., Gu W.-M., Zhao X.-H., Dai Z.-G., Lu J.-F., 2010, A&A, 516, A16
Lugones G., Horvath J. E., 2002, Phys. Rev. D, 66, 074017
Mallick R., Majumder S., 2009, Phys. Rev. D., 79, 023001
Mészáros P., Rees M. J., 1992, MNRAS, 257, 29
Miller W. A., George N. D., Kheyfets A., McGhee J. M., 2003, ApJ, 583, 833
Nozawa T., Stergioulas N., Gourgoulhon E., Eriguchi Y., 1998, A&A, 132, 431

Paczynski B., 1990, ApJ, 363, 218
Perez-Giz G., Levin J., 2009, Phys. Rev. D, 79, 124014
Rapp R., Schaffer T., Shuryak E. V., Velkovsky M., 2000, Ann. Phys. (N. Y.), 280, 35
Ruffert M., Janka H.-T., 1998, A&A, 338, 535
Ruffert M., Janka H.-T., 1999, A&A, 344, 573
Salmonson J. D., Wilson J. R., 1999, ApJ, 517, 895
Salmonson J. D., Wilson J. R., 2001, ApJ, 561, 950
Schnittman J. D., Bertschinger E., 2004, ApJ, 606, 1098
Shen H., Toki H., Oyamatsu K., Sumiyoshi K., 1998, Nucl. Phys. A, 637, 435
Shibata M., Sasaki M., 1998, Phys. Rev. D, 58, 104011
Stergioulas N., 2003, Living Rev. Rel., 6, 3
Stergioulas N., Friedman J. L., 1995, ApJ, 444, 306
Stergioulas N., Kluzniak W., Bulik T., 1999, A&A, 352, L116
Witten E., 1984, Phys. Rev. D, 30, 272
Zhang B., 2007, Chin. J. Astron. Astrophys., 7, 1
Zhang D., Dai Z. G., 2009, ApJ, 703, 461

APPENDIX A: PHYSICAL PARAMETERS OF NEUTRON AND QUARK STARS

Here, we present all the physical parameters of the compact stars with total mass $M \approx 1.8\,\mathrm{M}_\odot$, and different rotational frequencies, which were obtained by the RNS code. In the tables ρ_c is the central density, M is the gravitational mass, M_0 is the rest mass, R_e is the circumferential radius at the equator, Ω is the angular velocity, Ω_p is the angular velocity of a particle in circular orbit at the equator, T/W is the rotational-gravitational energy ratio, J is the angular momentum, I is the moment of inertia, Φ_2 gives the mass quadrupole moment, h_+ is the height from the surface of the last stable co-rotating circular orbit in the equatorial plane, h_- is the height from surface of the last stable counter-rotating circular orbit in the equatorial plane, Z_p is the polar redshift, Z_b is the backward equatorial redshift, Z_f is the forward equatorial redshift, ω_c/Ω is the ratio of the central value of the potential ω to Ω, r_e is the coordinate equatorial radius, and $r_\mathrm{p}/r_\mathrm{e}$ is the axes ratio (polar to equatorial), respectively.

We have obtained r_ms from the formula $r_\mathrm{ms} = R_\mathrm{e} + h_+$, i.e. as a sum of the stellar radius in the equator and the height from the surface of the last stable co-rotating circular orbit in the equatorial plane. Thus, the inner edge of the accretion disc is located at the radius of the innermost stable circular orbit r_ms, or at the equatorial radius R_e of the stellar surface, if h_+ is zero. In order to check the value of r_ms we have used a truncated form of the analytical approximation given by Shibata & Sasaki (1998),

$$r_\mathrm{ms} \approx 3r_g \left(1 - 0.54433a_* - 0.22619a_*^2 + 0.17989Q_2 - 0.23002a_*^3 + 0.26296a_*Q_2 - 0.29693a_*^4 + 0.44546a_*^2Q_2\right), \quad \text{(A1)}$$

where $a_* = cJ/GM^2$ and $Q_2 = c^4\Phi_2/G^2M^3$ are the dimensionless spin parameter and the dimensionless mass quadrupole moment, defined in terms of the angular momentum J and the mass quadrupole moment Φ_2.

Table A1. The physical parameters of neutron and quark star models calculated with the RNS code for a total mass of $1.8\,\mathrm{M}_\odot$ and angular velocity of $5 \times 10^3\,\mathrm{s}^{-1}$, for different types of EOSs.

EOS	DH	Stiff RMF	STOS 0	BBBAV14	BBBParis	APR	Q	CFL150
$\rho_\mathrm{c}\,(10^{15}\mathrm{g\,cm^{-3}})$	1.2940	0.5700	0.3690	2.1500	1.7000	1.2130	0.9310	0.7050
$M\,(\mathrm{M}_\odot)$	1.8071	1.8152	1.8541	1.8048	1.7989	1.8084	1.8072	1.8069
$M_0\,(\mathrm{M}_\odot)$	2.0569	2.0173	2.0155	2.1075	2.0948	2.0976	2.1047	2.0986
R_e(km)	12.009	15.909	21.039	10.350	10.707	11.408	11.833	12.464
$\Omega(10^4\mathrm{s}^{-1})$	0.4998	0.5074	0.4902	0.5041	0.5042	0.4940	0.4911	0.5065
$\Omega_\mathrm{p}(10^4\mathrm{s}^{-1})$	1.1613	0.7938	0.5372	1.4411	1.3705	1.2550	1.1994	1.1211
$T/W(10^{-2})$	0.0344	0.0928	0.1491	0.0238	0.0272	0.0332	0.0467	0.0577
$cJ/G\,\mathrm{M}_\odot^2$	1.1535	2.0742	2.9524	0.9538	1.0108	1.1319	1.3284	1.5341
$I(10^{45}\,\mathrm{g\,cm^2})$	2.0282	3.5925	5.2931	1.6627	1.7619	2.0137	2.3775	2.6619
$\Phi_2(10^{42}\,\mathrm{g\,cm^3})$	83.325	458.35	1061.9	43.101	53.793	79.055	136.07	198.87
h_+(km)	1.6748	0.0000	0.0000	3.3844	2.9361	2.2968	0.0000	0.0000
h_-(km)	7.4825	–	7.8498	8.3523	8.1702	8.0095	0.0000	0.0000
Z_p	0.3820	0.2945	0.2601	0.4695	0.4441	0.4086	0.3907	0.3704
Z_f	0.0262	−0.1178	−0.2296	0.1207	0.0955	0.0622	0.0443	0.0070
Z_b	0.7738	0.7492	0.7891	0.8605	0.8338	0.7945	0.7807	0.7814
$\omega_\mathrm{c}/\Omega(10^{-1})$	0.5865	0.4549	0.4102	0.6666	0.6342	0.5848	0.5293	0.4997
r_e(km)	9.0959	12.944	18.015	7.4081	7.7814	8.4743	8.8896	9.4976
$r_\mathrm{p}/r_\mathrm{e}$	0.8860	0.7200	0.5400	0.9250	0.9150	0.8980	0.8700	0.8350

Table A2. The physical parameters of neutron and quark star models calculated with the RNS code for a total mass of $1.8\,M_\odot$, and angular velocities of $3 \times 10^3\,s^{-1}$, and $4 \times 10^3\,s^{-1}$, respectively, for different types of EOSs.

EOS	Stiff RMF	Stiff RMF	APR	APR	Q	Q	CFL150	CFL150
$\rho_c\,(10^{15}\,g\,cm^{-3})$	0.6850	0.6400	1.2650	1.2400	1.0300	0.9800	0.7580	0.735
$M\,(M_\odot)$	1.8054	1.8000	1.8007	1.8059	1.8029	1.8015	1.8012	1.8021
$M_0\,(M_\odot)$	2.0336	2.0171	2.1000	2.1015	2.1146	2.1058	2.1098	2.1034
R_e(km)	14.037	14.609	11.052	11.203	11.391	11.581	11.932	12.140
$\Omega(10^4\,s^{-1})$	0.3004	0.4016	0.3018	0.4007	0.2994	0.3998	0.3021	0.4041
$\Omega_p(10^4\,s^{-1})$	0.9254	0.8785	1.3116	1.2864	1.2551	1.2283	1.1744	1.1514
$T/W(10^{-2})$	0.0237	0.0473	0.0115	0.0209	0.0155	0.0292	0.0184	0.0344
$cJ/G\,M_\odot^2$	0.9851	1.4065	0.6563	0.8930	0.7529	1.0357	0.8433	1.1644
$I(10^{45}\,g\,cm^2)$	2.8823	3.0779	1.9110	1.9584	2.2101	2.2767	2.4533	2.5323
$\Phi_2(10^{42}\,g\,cm^3)$	102.82	212.48	26.753	49.114	43.923	83.430	62.235	117.04
h_+(km)	0.0000	0.0000	3.3475	2.8157	0.0000	0.0000	0.0000	0.0000
h_-(km)	–	–	6.7995	7.4238	0.0000	0.0000	0.0000	0.0000
Z_p	0.2884	0.2896	0.4013	0.4052	0.3840	0.3860	0.3589	0.3635
Z_b	0.0640	−0.0170	0.1917	0.1258	0.1750	0.1066	0.1462	0.0775
Z_f	0.5260	0.6205	0.6252	0.7102	0.6082	0.6932	0.5873	0.6784
$\omega_c/\Omega(10^{-1})$	0.4697	0.4628	0.5877	0.5870	0.5359	0.5317	0.5005	0.4999
r_e(km)	11.175	11.725	8.159	8.2888	8.5039	8.6746	9.0429	9.2221
r_p/r_e	0.9225	0.8500	0.9640	0.9350	0.9549	0.9170	0.9450	0.8990

This paper has been typeset from a TEX/LATEX file prepared by the author.